Energies **2015**, *8*, 10958-10970; doi:10.3390/en81010958

OPEN ACCESS

energies

ISSN 1996-1073

www.mdpi.com/journal/energies

Article

Enhancing Thermoelectric Properties of $Si_{80}Ge_{20}$ Alloys Utilizing the Decomposition of $NaBH_4$ in the Spark Plasma Sintering Process

Ali Lahwal [1,*], Xiaoyu Zeng [1], Sriparna Bhattacharya [1,2], Menghan Zhou [1], Dale Hitchcock [1], Mehmet Karakaya [1,2], Jian He [1], Apparao M. Rao [1,2] and Terry M. Tritt [1,3,*]

1 Department of Physics & Astronomy, Clemson University, Clemson, SC 29634, USA; E-Mails: xzeng@g.clemson.edu (X.Z.); bbhatta@g.clemson.edu (S.B.); menghaz@g.clemson.edu (M.Z.); daleh@clemson.edu (D.H.); mkaraka@g.clemson.edu (M.K.); jianhe@g.clemson.edu (J.H.); arao@g.clemson.edu (A.M.R.)

2 Clemson Nanomaterials Center, and Center for Optical Materials Science and Engineering Technologies, Clemson University, Clemson, SC 29625, USA

3 Department of Materials Science & Engineering, Clemson University, Clemson, SC 29634, USA

* Authors to whom correspondence should be addressed; E-Mails: alahwal@g.clemson.edu (A.L.); ttritt@g.clemson.edu (T.M.T.); Tel.: +1-864-353-5085 (T.M.T.); Fax: +1-864-656-0805 (T.M.T.).

Academic Editor: Shi Xue Dou

Received: 17 July 2015 / Accepted: 14 September 2015 / Published: 29 September 2015

Abstract: The thermoelectric properties of spark plasma sintered, ball-milled, *p*-type $Si_{80}Ge_{20}$-$(NaBH_4)_x$ (x = 0.7,1.7 and 2.7), and $Si_{80}Ge_{20}B_{1.7-y}$-$(NaBH_4)_y$ (y = 0.2 and 0.7) samples have been investigated from 30 K to 1100 K. These samples were prepared by spark plasma sintering of an admixture of *Si*, *Ge*, *B* and $NaBH_4$ powders. In particular, the degasing process during the spark plasma sintering process, the combined results of X-ray powder diffraction, Raman spectroscopy, Hall coefficient, electrical resistivity, and Seebeck coefficient measurements indicated that $NaBH_4$ decomposed into *Na*, *B*, Na_2B_{29}, and H_2 during the spark plasma sintering process; *Na* and *B* were doped into the *SiGe* lattice, resulting in favorable changes in the carrier concentration and the power factor. In addition, the ball milling process and the formation of Na_2B_{29} nanoparticles resulted in stronger grain boundary scattering of heat-carrying phonons, leading to a reduced lattice thermal conductivity. As a result, a significant improvement in the figure of merit *ZT* (60%) was attained in *p*-type $Si_{80}Ge_{20}$-$(NaBH_4)_{1.7}$ and $Si_{80}Ge_{20}$-$B_{1.5}(NaBH_4)_{0.7}$ at 1100 K as compared

to the *p*-type B-doped $Si_{80}Ge_{20}$ material used in the NASA's radioactive thermoelectric generators. This single-step "doping-nanostructuring" procedure can possibly be applied to other thermoelectric materials.

Keywords: SiGe; thermoelectric; spark plasma sintering; power factor; thermal conductivity

1. Introduction

Thermoelectric materials are of technological interest owing to their ability of direct heat-to-electricity energy conversion. Currently, Silicon-Germanium (*SiGe*) alloys are the only thermoelectric materials that have found applications in power generation in the temperature range of 900 K < T < 1300 K [1,2]. Many efforts have been exerted to enhance the dimensionless thermoelectric figure of merit $ZT = (\alpha^2\sigma/\kappa)T$ of *SiGe* compounds [3,4], where α is the Seebeck coefficient, σ the electrical conductivity, κ the thermal conductivity, T the absolute temperature, and $PF = \alpha^2\sigma T$ the power factor. The *p*-type (*Boron, B*-doped) and *n*-type (*Phosphorus*, *P*-doped) *SiGe* material used in NASA's radioisotope thermoelectric generators (RTGs) possess a ZT of 0.5 and 0.9, respectively [2]. In the past few decades, there have been many theoretical [5–7] and experimental efforts [8–11] toward further enhancing the ZT of *SiGe* via an enhancement of the PF and/or a reduction in κ. Some results are noteworthy. For example, particle size distribution was found to be crucial to achieve dense homogeneous samples [12]; polycrystalline *SiGe* possesses a better thermoelectric performance than single crystalline *SiGe* [13]; mechanical ball milling is effective in producing single phased *SiGe* powder [14,15]. A significant improvement in ZT with peak values about 1.3 and 0.95 at 1200 K in *n-type* and *p-type* respectively were achieved via reducing the lattice thermal conductivity (κ_L) using a high energy ball milling method to produce nanostructured SiGe [11,16]. Recently we have employed the spark plasma sintering (SPS) technique to synthesize high relative density *SiGe* directly from single elemental (SE) *Si* and *Ge* powders, which possess thermoelectric performance comparable to those used in NASA's RTGs [17].

Doping plays a central role in optimizing the thermoelectric performance of *SiGe* as dopants optimize the carrier concentration while simultaneously acting as point defects which can strongly scatter the heat-carrying phonons at elevated temperatures. Previously the effects of different dopants, including *P*, *Ga*, *B*, *GaP*, *In*, *Sb*, and *InSb*, on the thermoelectric properties of $Si_{80}Ge_{20}$ alloys have been investigated [18,19]. Doping typically governs the PF, which is at the core and often the bottle-neck of enhancing ZT in many thermoelectric materials. It is generally accepted that a strongly energy-dependent differential electrical conductivity leads to enhancement of the PF [20]. Such strong energy dependence arises from the density of states and/or from the relaxation time of charge carriers [21,22]. In addition to doping, the "compositing or nanostructuring" process is another way to enhance the PF. Bergman and Fel showed that the PF could be enhanced by making a two-phase composite in a parallel slab micromorphology or a core-shell micromorphology [23]. Doping and nanostructuring combined in this modulation-doping approach to enhance the PF. For example, the PF of *p*-type $Si_{80}Ge_{20}B_{1.5}$ was improved by a factor of 40% by embedding 30 vol. % *B*-doped *SiGe* nanoparticles in the intrinsic *SiGe* host matrix to form $(Si_{80}Ge_{20})_{0.7}(Si_{100}B_5)_{0.3}$ composites [24]. Furthermore, grain boundary engineering is

another effective approach to enhancing the *PF* in several cases. For example, the alkali metal salt $NaBH_4$ processing appears to lead to thermoelectrically-favorable grain boundaries in *p*-type Bi_2Te_3 [25] and $Pb_{0.75}Sn_{0.25}Te$ [26].

In this work, we have simultaneously achieved *Na*-doping, *B*-doping, formation of Na_2B_{29} nanoparticles, and sample densification via the decomposition of $NaBH_4$ in a single-step synergistic "doping-nanostructuring-sintering" process. As a result, the *PF* is enhanced while the total thermal conductivity, κ, is reduced, thereby leading to a significantly enhanced *ZT*.

2. Experimental Results and Data Analyses

In this work, doping is achieved via decomposition of $NaBH_4$ in the SPS process. Three samples were treated with sodium boron hydride $(NaBH_4)_x$ (x = 0.7, 1.0, and 2.7), while two samples were treated with single element boron (*B*) in addition to sodium boron hydride $B_{1.7-y}(NaBH4)_y$ (y = 0.2 and 0.7). The purpose of preparing the $Si_{80}Ge_{20}B_{1.5}(NaBH_4)_{0.2}$ and $Si_{80}Ge_{20}B_1(NaBH_4)_{0.7}$ sample with increasing percentage of $NaBH_4$ and decreasing *B*, is to investigate the extent of the $NaBH_4$ decomposition with the same total amount of *B*.

In general, the thermal decomposition of $NaBH_4$ follows:

$$NaBH_4 \rightarrow \sum_i solid_i(Na, B, H) + \sum_j gas_j(B, H)$$

where the products can be single elemental *Na*, *B*, H_2, or binary phases, e.g., *Na–B* such as Na_2B_{29}, Na_2B_{30}, Na_3B_{20} or *Na–H*, or ternary phases, *Na–B–H* [27].

The thermal decomposition of $NaBH_4$ occurs between 600 °C and 700 °C [27], significantly below our SPS temperature of 1020 °C. Indeed, we observed the presence of *B*-rich *Na–B* compounds namely Na_2B_{29} by SEM, EDX, and XRD measurements. Importantly, degasing was observed in spark plasma sintering $NaBH_4$-added *SiGe* samples, but not in $NaBH_4$-free samples, confirming the formation of H_2. An immediate question arises as to where exactly the *Na* resides after this decomposition. Figure 1a shows the XRD pattern of $NaBH_4$ –added $Si_{80}Ge_{20}$ alloys after the SPS process. The lattice constant was determined using the (111) and (220) peaks by Bragg's law. The peaks from Na_2B_{29} were observed and marked with asterisk in Figure1a. The ICSD PDF file number of Na_2B_{29} is 01-071-2824, and the space group is I 1 m 1 [27]. No other secondary phases were observed.

Interestingly, the XRD peaks of the sample treated with *B* and $NaBH_4$ $\{Si_{80}Ge_{20}B_{1.5}(NaBH_4)_{0.2}\}$ shifted to higher angle, contrary to those samples treated with only $NaBH_4$ $\{Si_{80}Ge_{20}(NaBH_4)_{1.7}\}$, indicating that the dominant dopant is *B*. The peak of the sample treated with only $NaBH_4$ $\{Si_{80}Ge_{20}(NaBH_4)_{1.7}\}$, on the other hand, is shifted to lower angle, consistent with a dominant *Na* doping (Figure 1b). This opposite shifting is attributed to the ionic radii of the *Na* (99 pm) and *B* (35 pm) comparing to Si or Ge (39 pm) [28]. Shifts of Raman peaks track with those of XRD peaks, confirming the doping by *Na* and *B* in the *SiGe* host matrix (Figure 1c). The decomposition of *NaBH4* in the SPS process opens a new way to dope *Na* into the *SiGe* host matrix, which is actually a $(Si_{80}Ge_{20})$ *composition*.

The TEM image (Figure 2a) shows that the ball milled admixture of *Si* and *Ge* powders has grain size from 0.3 to 1.0 μm, compared to 1–20 μm and 44 μm for pristine *Si* and *Ge* powders before the ball milling process. Despite the grain coarsening during the SPS process in each sample, we adopted the

same ball milling and SPS conditions for all samples; it is, thus, plausible to assume the grain size of *SiGe* coarse grains should be nearly the same for all samples after SPS process, which is a fixed parameter in our study of the doping effects. Figure 2b shows the Na_2B_{29} nanoparticles on the grain boundaries of *SiGe* host matrix grains.

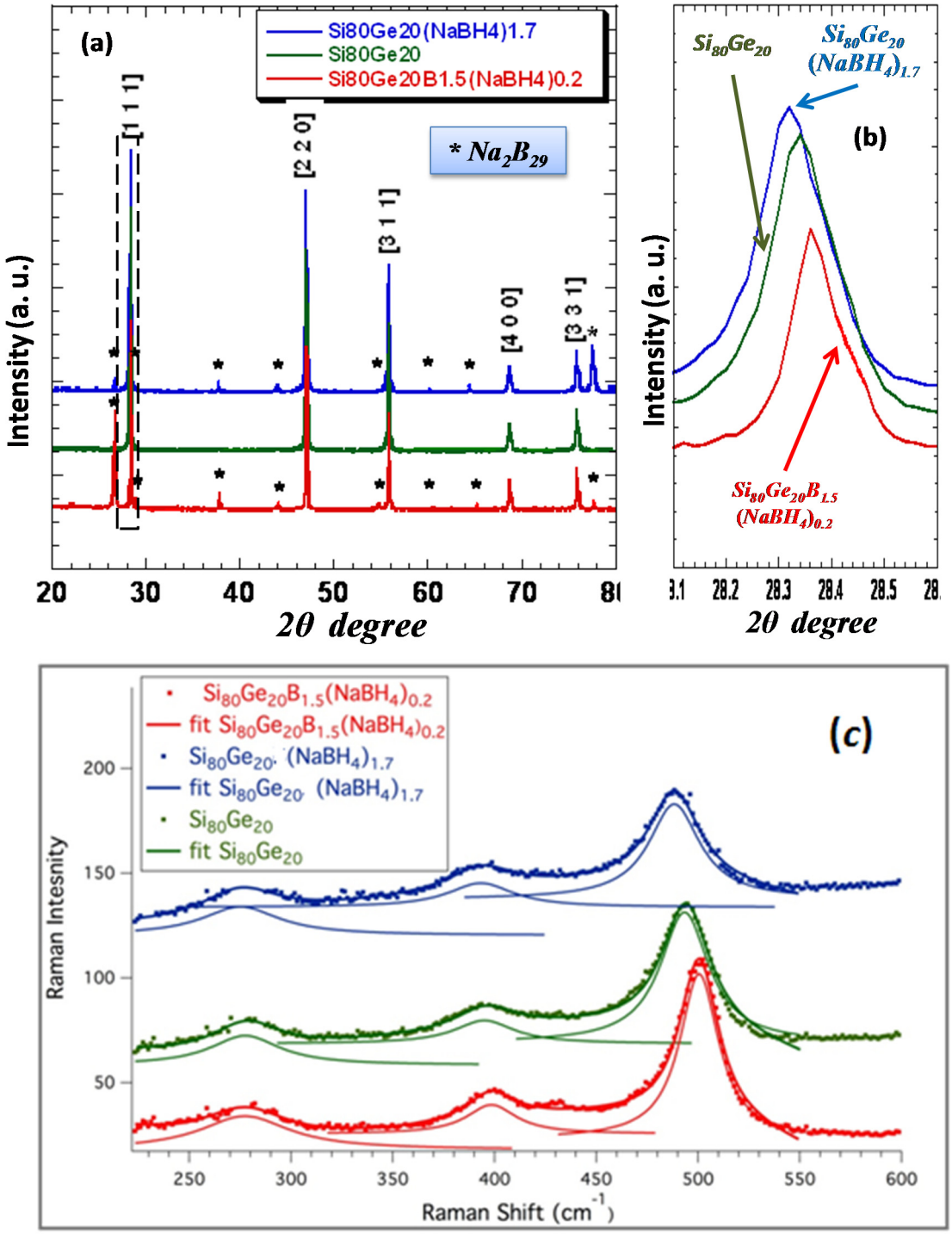

Figure 1. (**a**) XRD patterns of the sample dominantly doped with B, the sample doped dominantly with Na, and pristine *SiGe*; (**b**) magnification of the (111) peak shift upon the Na and B doping, note that the peaks shift to the opposite direction; and (**c**) Raman peak shifting tracks with XRD peak shifting.

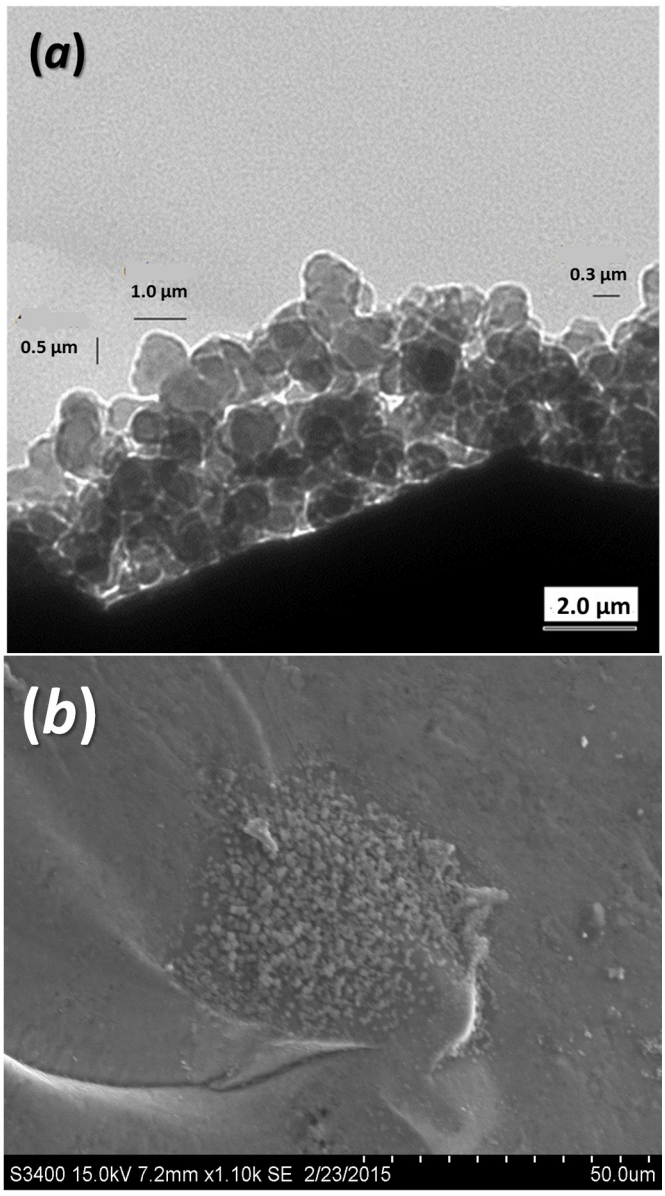

Figure 2. (**a**) TEM image shows the grain size of ball milled *SiGe* powder before SPS; and (**b**) SEM image of a fracture surface shows the agglomerate of Na_2B_{29} nanoparticles at the grain boundary.

Figure 3a–c present the temperature dependence of the electrical resistivity Seebeck coefficient, and power factor α^2/ρ, respectively, of the dense bulk $NaBH_4$-treated *p*-type $Si_{80}Ge_{20}$ in comparison to the *p*-leg material used in NASA's RTGs [2]. All of the samples exhibit similar trends in the temperature dependence of their physical properties. The sign of the Seebeck coefficient and that of the Hall coefficient confirm a *p*-type conduction. As shown in Figure 3b, the Seebeck coefficient, of most of the as-prepared samples, rivals that of the reference (*i.e.*, the *p*-leg material used in NASA RTGs), except the 2.7% $NaBH_4$ sample that shows a lower α. Since the Seebeck coefficient is positively correlated to the effective mass m^*, and inversely proportional to the carrier concentration *n*, one possible explanation for the decreased α in the sample with 2.7% $NaBH_4$ is the increasing of *n*. A significant enhancement in the *PF*, compared to the reference, is attained for all the samples (see Figure 3c).

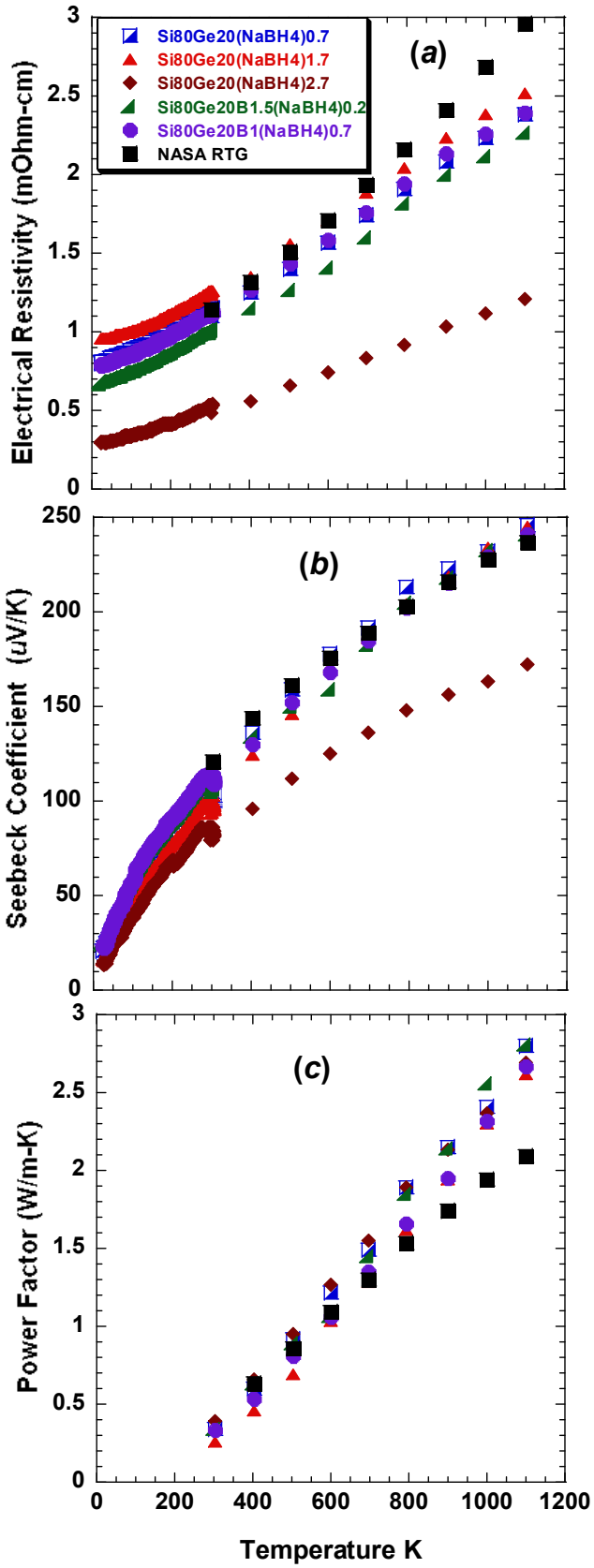

Figure 3. Temperature dependence of (**a**) the electrical conductivity; (**b**) Seebeck coefficient; and (**c**) power factor α^2T/ρ, of five SPS prepared nanostructured dense bulk $Si_{80}Ge_{20}$ alloy samples doped with $(NaBH_4)_x$ (x = 0.7,1.7 and 2.7) and $B_{1.7-y}(NaBH_4)_y$ (y = 0.2 and 0.7) in comparison to the p-leg material used in NASA's RTGs.

The carrier concentration of *p*-type $Si_{80}Ge_{20}$ is about 1.67 × 10^{20} cm^{-3} [11,13]. The decrease of the electrical resistivity ρ for the samples can be explained in terms of the increasing of both the carrier concentration *n* and the Hall mobility (*n* ~ 2.5 × 10^{20} cm^{-3} and μ ~ 34 $cm^2 \cdot V^{-1} \cdot s^{-1}$), especially for the sample treated with 2.7% $NaBH_4$ that has higher *n* and μ (*n* ~ 4×10^{20} cm^{-3} and μ ~ 40 $cm^2 \cdot V^{-1} \cdot s^{-1}$ at room temperature), as shown in Figure 4a,b. The carrier concentration exhibits an essentially temperature-independent behavior, while the mobility shows a weak, but well-discerned, negative temperature coefficient. Among the conventional scattering mechanisms, such as the charge carrier-phonon scattering, charge carrier-charge neutral point defect scattering, charge carrier-charged point defect scattering, and charge carrier-grain boundary, only the charge carrier-phonon scattering mechanism gives rises to a negative temperature coefficient [29]. Hence, we conclude that the charge carrier-phonon scattering is the dominant carrier scattering mechanism, though the charged and charge neutral point defects may coexist. Note that the magnitude change of the carrier concentration agrees with a hole-doping scenario, as expected for the Na-doping and B-doping.

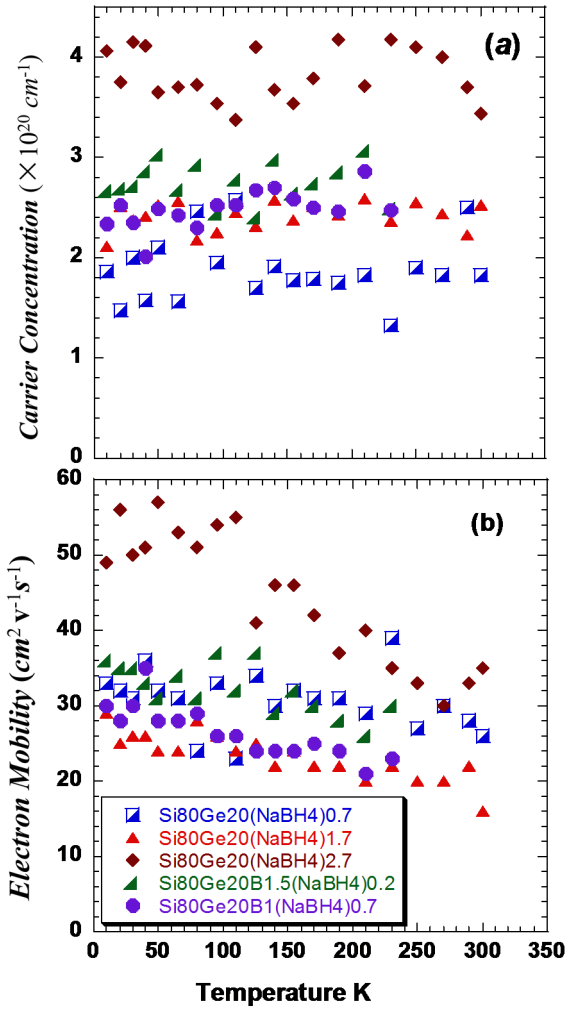

Figure 4. (**a**) Temperature dependent of carrier concentration, n; and (**b**) Hall mobility, μ.

Figure 5a shows the temperature dependent total thermal conductivity of all the samples. With the exception of the $Si_{80}Ge_{20}(NaBH_4)_{2.7}$ sample the composited samples have lower total thermal conductivity than the reference. The sample treated with 2.7% $NaBH_4$ shows a higher thermal

conductivity than that of the reference, which is attributed to the large electronic thermal conductivity κ_e (Figure 5b). The electronic thermal conductivity is estimated by the Wiedemann-Franz relation and subtracted from the total thermal conductivity to derive the lattice thermal conductivity. The lattice thermal conductivity κ_L as a function of temperature is plotted in Figure 5c. Once again, the reference has the highest κ_L, while the $Si_{80}Ge_{20}(NaBH_4)_{1.7}$ sample shows the lowest lattice thermal conductivity. The lattice thermal conductivity is reduced due to an increase in the number of grain boundaries [30] by ball milling and the formation of nanoparticles, and the extra point defects introduced by the Na and B dopants. The best result was attained by $(NaBH_4)_{1.7}$ treatment whose thermal conductivity is ~20%–25% lower than the reference over a wide temperature range between 300 K and 1100 K.

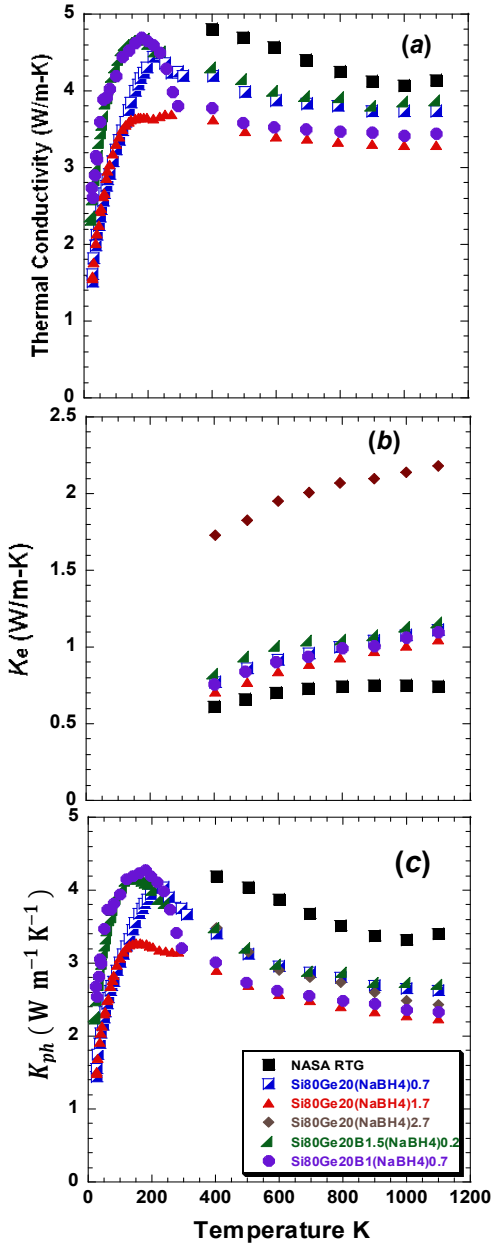

Figure 5. Temperature dependence of (**a**) the total thermal conductivity; (**b**) the electronic thermal conductivity; and (**c**) the lattice thermal conductivity.

As mentioned earlier, the purpose of treating two samples with *B* and $NaBH_4$ {$Si_{80}Ge_{20}B_{1.5}(NaBH_4)_{0.2}$ and $Si_{80}Ge_{20}B_1(NaBH_4)_{0.7}$} with increased percentage of $NaBH_4$ and decreased *B*, is to investigate whether $NaBH_4$ completely decomposes to only *B*, *Na*, and H_2 or also to boron-rich sodium phase. We found that increasing the $NaBH_4$ percentage leads to a larger reduction in the total and lattice thermal conductivities without a degradation of the electrical properties, which can be correlated with the increasing amount of Na_2B_{29} nanoparticles at the grain boundaries. For example, the lowest thermal conductivity of $Si_{80}Ge_{20}(NaBH_4)_{1.7}$ sample that has most Na_2B_{29} has the lowest lattice thermal conductivity. Figure 2b shows the Na_2B_{29} nanoparticles imbedded in the fracture surface of the sample after SPS, where numerous nanoparticles with a size ~20 nm have emerged at the grain boundary. As the percentage of $NaBH_4$ is increased (consequently increased Na_2B_{29}) the peak of the lattice thermal conductivity decreased especially for the $Si_{80}Ge_{20}(NaBH_4)_{1.7}$ sample that has a higher concentration of boron-rich sodium nanoparticles.

Dimensionless figure of merit *ZT* values higher than those of NASA's RTG materials were attained (Figure 6) for all of the samples studied. This enhancement can be attributed to the enhancement in the *PF* and also the reduction of thermal conductivity, especially the lattice component. The *ZT* value of $Si_{80}Ge_{20}$-$(NaBH_4)_{1.7}$ and $Si_{80}Ge_{20}$-$B_{1.5}(NaBH_4)_{0.2}$ shows a maximum of about 0.8 at 1100 K, which is about 45% higher than that of the *p*-leg material of NASA's RTG (*ZT* ~ 0.5).

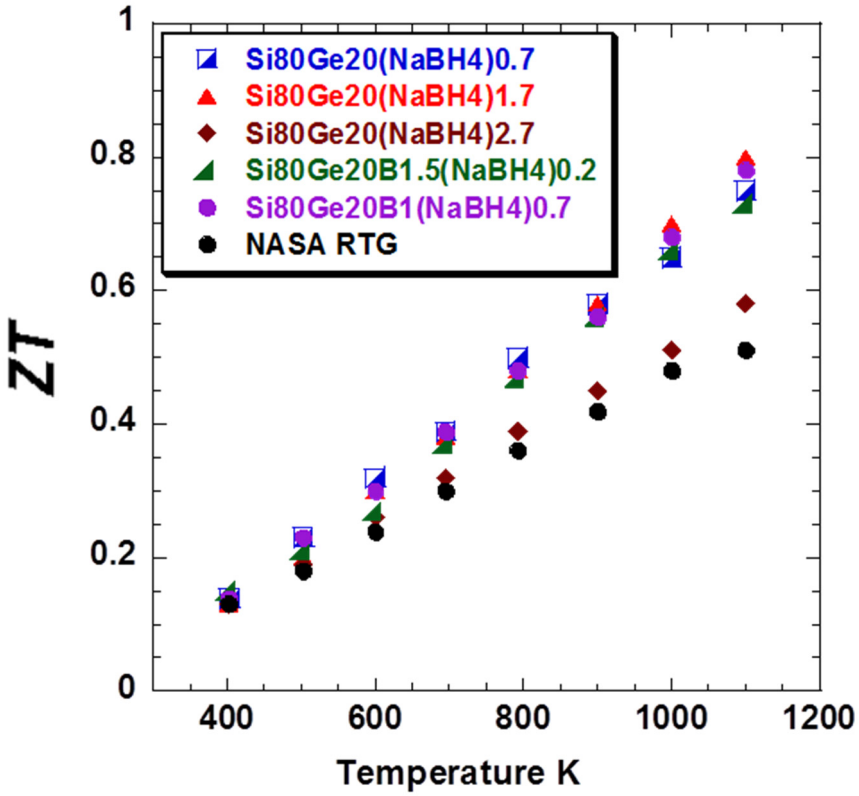

Figure 6. Dimensionless figure of merit ZT of all the samples compared to the p-leg material of NASA's RTG.

3. Experimental Details

$Si_{80}Ge_{20}$ alloys were fabricated by ball milling (BM) process followed by spark plasma sintering (SPS) procedure, which is both time- and cost-efficient, and easy to scale up. Small grain size powders were selected: 1–20 μm silicon powder (99.9985% Alfa Aesar®, 26 Parkridge Rd, Ward Hill, MA 01835, USA) and germanium powder −100 mesh (Alfa Aesar® 99.999%) and used in this process. To avoid oxidation, the powders were loaded into a milling container inside a glove box. Then the powders were ball milled for 12 h to further refine the grains and thoroughly mix the powders. The ball milled powders were then divided into five batches, mixed with appropriate amount of $NaBH_4$ and B according to the nominal formulas $Si_{80}Ge_{20}(NaBH_4)_x$ and $Si_{80}Ge_{20}\ B_{1.7-y}(NaBH_4)_y$, where x = 0.7, 1.7, 2.7, y = 0.2 and 0.7 in a 3-D mixer. These samples were sintered using a Dr. Sinter SPS-515S (Fuji Electronic Industrial Co.®) (Tokyo, Japan) and characterized regarding their thermoelectric properties [17]. The Archimedes method measurements showed that the densities of the as-pressed samples were least 98% of the theoretical density (2.99 ± 0.1 g/cc).

The phase purity and micromorphology of these samples before and after SPS were then characterized by X-ray diffraction (XRD) using a Rigaku® Miniflex, The Woodlands, TX, USA) and Hitachi® S-3400N (Hitachi America, Troy, NY USA) equipped with an Oxford X-act® energy dispersive X-ray spectroscopy (EDX). Oxford Instruments, Raleigh, NC, USA) In order to investigate the effect of the dopants, Raman spectra were acquired with Dilor® XY triple grating (Dilor®, Lille, France) and Renishaw® InVia Raman microscopes (Renishaw Inc.®, Hoffman Estates, IL, USA) with E_{laser} = 2.33 eV. The incident laser beam was focused using a 50× objective, and the laser power on the samples was kept to a minimum to avoid heating. The thermal diffusivity measurements were performed on the densified pellet with 12.7 mm diameter and 2 mm thickness before cutting to approximately 10 × 2 × 2 mm^3 bars for other transport measurements. High-temperature thermal diffusivity measurements were made on a Netzsch® LFA 457 (Burlington, MA, USA) laser flash apparatus using the transient method from 300 K to 1100 K. The high-temperature thermal conductivity of the samples was calculated using $\kappa = d\ D\ C_V$, where d is the thermal diffusivity, D the density and C_V the specific heat at constant volume. The high-temperature specific heat at constant pressure, C_P, was measured on a Netzsch® (Burlington, MA USA) differential scanning calorimeter 404 "Pegasus". The specific heat at constant pressure, C_P, and the specific heat at constant volume, C_V, were considered to be essentially the same for the calculation of the total thermal conductivity. High-temperature resistivity ($\rho = 1/\sigma$) and Seebeck coefficient were measured using the commercially-available Ulvac® ZEM-3 (Boston, MA, USA) from 300 K to 1100 K. The low temperature thermal conductivity was measured, on the same samples, from ~ 10 K to room temperature using a custom-designed steady-state technique [31]. The lattice thermal conductivity (κ_L) was obtained by applying the Wiedemann–Franz relationship, $\kappa_e = L_0 \sigma T$, with the Lorenz number for a degenerate semiconductor, $L_0 = 2 \times 10^{-8}$ W Ω/K^2, σ the electrical conductivity, and the formula $\kappa_L = \kappa_{total} - \kappa_e$. The low temperature Seebeck coefficient and electrical resistivity were measured on a custom-designed system from 30 K to 300 K [32]. Hall-effect measurements were performed on a Quantum Design® (San Diego, CA, USA) physical properties measurement system (PPMS) using a five-probe configuration by sweeping the magnetic field between ±1 Tesla, and the carrier concentration was calculated from the Hall data $R_H = 1/ne$, where R_H is the Hall coefficient, e the electron charge, and n the carrier concentration. The electron mobility was then calculated from

$\mu = R_H/\rho$. Additionally a thermal stability test was carried out by annealing the samples at 1100 K for 48 h in evacuated tubes before reinvestigating their thermoelectric properties. Importantly, no significant degradation of the physical properties was found.

4. Conclusions

We successfully reduced the lattice thermal conductivity and enhanced the power factor of *p*-type *SiGe* alloys via decomposing $NaBH_4$ and densifying samples in a single-step spark plasma sintering process. The decomposition of $NaBH_4$ led to *Na* and *B* doping into the *SiGe* lattice and the formation of Na_2B_{29} nanoparticles on the grain boundary of *SiGe* coarse grain. The reduction of the electrical resistivity is attributed to the increased carrier concentration. The reduction in the lattice thermal conductivity is mainly due to enhanced phonon scattering due to the increased point defect scattering, the increased number of grain boundaries, as well as the scattering from the boron-rich sodium nanoparticles. The present work presents a new method for doping *Na* into *SiGe*, which can, in principle, be extended to other alkali metal salts and in other existing thermoelectric materials.

Acknowledgments

Ali Lahwal acknowledges a special program of Ministry of Higher Education funded by the Libyan Government. We also acknowledge the early contributions of Daniel Thompson while at Clemson University and currently at General Motors R&D. Menghan Zhou, Dale Hitchcock, and Jian He would like to acknowledge the support of NSF DMR 1307740. Terry M. Tritt would like to acknowledge a support under a DoE subcontract with Nanosonics Inc. (Blacksburg, VA).

Author Contributions

Ali Lahwal measured the thermoelectric properties, analyzed the data of the thermoelectric properties and Hall measurements and drafted the manuscript.

Xiaoyu Zeng, and Menghan Zhou contributed in measuring the low and high temperature measurements of the thermal conductivity, Seebeck coefficient and electrical resistivity.

Sriparna Bhattacharya contributed in XRD and DES analysis.

Dale Hitchcock and Jian He contributed in Hall coefficient measurements and reviewing the results and the manuscript.

Mehmet Karakaya and Apparao M. Rao conducted the Raman measurements and data analysis.

Terry M. Tritt designed the instruments and reviewed the results and the manuscript.

Conflicts of Interest

The authors declare no conflict of interest.

References

1. Wood, C. Materials for Thermoelectric Energy Conversion. *Rep. Prog. Phys*. **1988**, *51*, 459–539.
2. Vining, C.B. Silicon Germanium. In *CRC Handbook of Thermoelectrics*; Rowe, D.M., Ed.; CRC Press: Boca Raton, FL, USA, 1995; pp. 329–338.

3. Bhandari, C.M.; Rowe, D.M. Silicon–Germanium Alloys as High-Temperature Thermoelectric Materials. *Contemp. Phys*. **1980**, *21*, 219–242.
4. Vining, C.B. A Model for the High-Temperature Transport Properties of Heavily Doped n-Type Silicon-Germanium Alloys. *J. Appl. Phys*. **1991**, *69*, 331–341.
5. Hicks, L.D.; Dresselhaus, M.S. Thermoelectric Figure of Merit of a One-Dimensional Conductor. *Phys. Rev*. *B* **1993**, *47*, 16631–16634.
6. Chen, G. Phonon Transport in Low Dimensional Structures. In *Recent Trends in Thermoelectric Materials Research III*; Semiconductors and Semimetals; Tritt, T.M., Ed.; Academic: New York, NY, USA, 2001; Volume 71, pp. 203–259.
7. Venkatasubramanian, R. Phonon Blocking Electron Transmitting Superlattice Structures as Thin Film Thermoelectric Materials. In *Recent Trends in Thermoelectric Materials Research III*; Semiconductors and Semimetals; Tritt, T.M., Ed.; Academic: New York, NY, USA, 2001; Volume 71, pp. 175–201.
8. Venkatasubramanian, R.; Siivola, E.; Colpitts, T.; O'Quinn, B. Thin-Film Thermoelectric Devices with High Room-Temperature Figures of Merit. *Nature* **2001**, *413*, 597–602.
9. Poudeu, P.F.P.; D'Angelo, J.; Downey, A.D.; Short, J.L.; Hogan, T.P.; Kanatzidis, M.G. Nanostructures versus Solid Solutions: Low Lattice Thermal Conductivity and Enhanced Thermoelectric Figure of Merit in $Pb_{9.6}Sb_{0.2}Te_{10-x}Se_x$ Bulk Materials. *J. Am. Chem. Soc.* **2006**, 128, 14347–14355.
10. Hochbaum, A.I.; Chen, R.; Delgado, R.D.; Liang, W.; Garnett, E.C.; Najarian, M.; Majumdar, A.; Yang, P. Enhanced thermoelectric performance of rough silicon nanowires. *Nature* **2008**, *451*, 163–167.
11. Wang, X.W.; Lee, H.; Lan, Y.C.; Zhu, G.H.; Joshi, G.; Wang, D.Z.; Yang, J.; Muto, A.J.; Tang, M.Y.; Klatsky, J.; *et al*. Enhanced thermoelectric figure of merit in nanostructured n-type silicon germanium bulk alloy. *Appl. Phys. Lett*. **2008**, *93*, 193121.
12. Baughman, R.J.; McVay, G.L; Lefever, R.A. Preparation of hot-pressed silicon germanium ingots: Part I–III. *Mater. Res. Bull.* **1974**, *9*, 685–692, 735–744, 863–872.
13. Vining, C.B.; Laskow, W.; Hanson, J.; van der Beck, R.R.; Gorsuch, P. Thermoelectric properties of pressure-sintered $Si_{0.8}Ge_{0.2}$ thermoelectric alloys. *J. Appl. Phys.* **1991**, *69*, 4333–4340.
14. Cook, B.A.; Harringa, J.L.; Han, S.H.; Beaudry, B.J. Parasitic, effects of oxygen on the thermoelectric properties of $Si_{80}Ge_{20}$ doped with GaP and P. *J. Appl. Phys*. **1992**, *72*, 1423–1428.
15. Cook, B.A.; Harringa, J.L.; Han, S.H.; Vining, C.B. $Si_{80}Ge_{20}$ thermoelectric alloys prepared with GaP additions. *J. Appl. Phys.* **1995**, *78*, 5474–5480.
16. Joshi, G.; Lee H.; Lan, Y.C.; Wang, X.W.; Zhu, G.H.; Wang, D.Z.; Gould, R.W.; Cuff, D.C.; Tang, M.Y.; Dresselhaus, M.S.; *et al*. Enhanced thermoelectric figure-of-merit in nanostructured p-type silicon germanium bulk alloys. *Nano Lett*. **2008**, *8*, 4670–4674.
17. Thompson, D.; Hitchcock, D.; Lahwal, A.; Tritt, T.M. Single-element spark plasma sintering of silicon germanium. *Emerg. Mater. Res.* **2012**, *1*, 299–305.
18. Ying, G.; Jiang, H.; Zhang, C.; Wu, X.; Niu, S. Thermoelectric properties on n-type $Si_{80}Ge_{20}$ with different dopants. In Proceedings of the 25th International conference of Thermoelectrics, Vienna, Austria, 6–10 August 2006; pp. 272–275.

19. Pisharody, P.K.; Garvey, L.P. Modified silicon-germanium alloys with improved performance. In Proceedings of the 7th Intersociety Energy Conversion Engineering Conference, San Diego, CA, USA, 20–25 August 1978; IEEE: New York, NY, USA, 1978; pp. 1963–1968.
20. Ravich, Y.I. Selective Carrier Scattering in Thermoelectric Materials. In *CRC Handbook of Thermoelectrics*; Rowe, D.M., Ed.; CRC Press: Boca Raton, FL, USA, 1995; pp. 67–81.
21. Heremans, J.P.; Jovovic, V.; Toberer, E.S.; Saramat, A.; Kurosaki, K.; Chroenphakdee, A.; Yamanaka, S.; Snyder G.F. Enhancement of thermoelectric performance in PbTe by distortion of the electronic density of states. *Science* **2008**, *321*, 554–557.
22. Jeong, C.; Lundstorm, M. On electronic structure engineering and thermoelectric performance. *J. Electron. Mater.* **2011**, *40*, 738–743.
23. Bergman, D.J.; Fel, L.G. Enhancement of thermoelectric power factor in composite thermoelectrics, *J. Appl. Phys.* **1999**, *85*, 8205–8216.
24. Zehbarjadi, M.; Joshi, G.; Zhu, G.; Yu, B.; Minnich, A.; Lan, Y.C.; Wang, X.; Dresselhaus, M.S.; Ren, Z.F.; Chen, G. Power Factor Enhancement by Modulation Doping in Bulk Nanocomposites. *Nano Lett.* **2011**, *11*, 2225–2230.
25. Ji, X.; He, J.; Su, Z.; Gothard, N.; Tritt, T.M. Improved thermoelectric performance in polycrystalline p-type Bi_2Te_3 via an alkali metal salt hydrothermal nanocoating treatment approach. *J. Appl. Phys.* **2008**, *104*, 0349071–0349076.
26. Ji, X.; Zhang, B.; Su, Z.; Holgate, T.; He, J.; Tritt, T.M. Nanoscale granular boundaries in polycrystalline $Pb_{0.75}Sn_{0.25}Te$: An innovative approach enhance the thermoelectric figure of merit. *Phys. Status Solidi A* **2009**, *206*, 221–228.
27. Martelli, P.; Caputo, R.; Remhof, A.; Mauron, P.; Borgschulte, A.; Zuttel, A. Stability and Decomposition of $NaBH_4$. *J. Phys. Chem. C* **2010**, *114*, 7173–7177.
28. Dean, J.A. *Lange's Handbook of Chemistry*; McGraw-Hill Inc.: New York, NY, USA, 1999; pp. 313–323.
29. Nag, B.R. *Electron Transport in Compound Semiconductors*; Springer: Berlin/Heidelberg, Germany, 1980; p. 30.
30. Klemens, P.G. Phonon scattering and thermal resistance due to grain boundaries. *Int. J. Thermophysics* **1994**, *15*, 1345–1351.
31. Pope, A.L.; Zawilski, B.M.; Tritt, T.M. Description of removable sample mount apparatus for rapid thermal conductivity measurements. *Cryogenics* **2001**, *14*, 725–731.
32. Pope, A.L.; Littleton, R.T., IV; Tritt, T.M. Apparatus for the rapid measurement of electrical transport properties for both "needle-like" and bulk materials. *Rev. Sci. Instrum.* **2001**, *72*, 3129–3131.